



Preparation, characterization of N–I co-doped TiO₂ and catalytic performance toward simultaneous Cr(VI) reduction and benzoic acid oxidation



A.E. Giannakas, M. Antonopoulou, Y. Deligiannakis, I. Konstantinou*

Department of Natural Resources and Environmental Management, University of Western Greece, G. Seferi 2, Agrinio 30100, Greece

ARTICLE INFO

Article history:

Received 22 February 2013

Received in revised form 19 April 2013

Accepted 23 April 2013

Available online 6 May 2013

Keywords:

N–I co-doped TiO₂

Cr(VI) reduction

Benzoic acid oxidation

EPR

N_b[•] species

ABSTRACT

Four N–I co-doped TiO₂ catalysts having Ti:N/I molar ratios of 1:1, 1:3, 1:5 and 1:10 were prepared via a sol–gel method using NH₄I as N–I dopant precursor. A pure TiO₂ (undoped) sample was also prepared by the same method for comparison. The catalysts were evaluated for the simultaneous photocatalytic reduction of Cr(VI) and oxidation of benzoic acid (BA). TiO₂ anatase phase was formed for all N–I co-doped catalysts as shown by XRD. UV–vis diffuse reflectance spectra showed that N–I co-doping resulted in increased absorption at visible wavelengths and a decrease of the band gap energy (E_g). The smallest E_g value of 2.34 eV was observed for the 1:5 Ti:N/I molar ratio. The structure and photodynamics of the TiO₂ catalysts was investigated in detail by Electron Paramagnetic Resonance (EPR) spectroscopy. The EPR data showed: [i] formation of non-photoactive NO centers and photoinduced N_b[•] paramagnetic species as a result of N doping, [ii] photoinduced Ti³⁺ surface ions, and [iii] formation of surficial oxygen O₂^{•−} radical ions and trapped holes TiO₄^{•+}–O^{•−}. The N_b[•] species act upon the narrowing of the band gap and the production of photogenerated electrons, i.e. Ti³⁺ surface ions. These Ti³⁺ surface ions have a key role, capturing gas O₂ and supporting both reduction and oxidation process. Cr(VI) reduction by the N–I co-doped catalysts followed the trend: TN15 > TN10 > TN1 > TN3 > TiO₂[undoped] which correlates with the concentration of N_b[•] species formed and the narrowing of E_g values. Oxidation of benzoic acid (BA) followed a more complex trend as follows: TN1 > TN3 > TN10 > TN15 which is the reverse of the trend for trapped holes TiO₄^{•+}–O^{•−}. Finally progressive microwave EPR saturation experiments show that N_b[•] species are located deeper in the TiO₂ lattice in particles with narrower E_g values.

© 2013 Elsevier B.V. All rights reserved.

1. Introduction

During the last two decades significant research efforts have been focused on TiO₂ as a promising photocatalyst. Compared with other semiconductors, TiO₂ is chemically stable, highly active, photo-corrosion resistant and low cost [1], resulting in its wide application [2]. However, the large band gap of TiO₂ (3.2 eV for anatase and 3.0 eV for rutile) is the main drawback [3] since it results in TiO₂ photoexcitation only by high-energy ultraviolet (UV) light ($\lambda < 400$ nm).

In order to use the green, abundant and cheap solar energy many attempts have been made to improve the optical response of TiO₂ under visible-light excitation. In recent years, since the report of Asahi et al. in 2001 [4], nonmetal doping of TiO₂ rekindled a great interest in visible-light photocatalysis. Since then, both the preparation methods and theoretical calculations have been performed

for nonmetal doping of TiO₂, e.g. with N [5], C [6], S [7], I [8–10], F [11]. Currently, there are three main different strategies regarding the light-absorption modification mechanism of TiO₂ [12]: (1) band gap narrowing, (2) introduction of impurity energy levels, and (3) creation of lattice-oxygen vacancies.

Recently, non-metal co-doping of TiO₂, e.g. by N–F [12,13], N–S [14], N–Br [15], N–I [16], C–N [17] emerged as a further leap forward. So far, among all co-doped materials N–F co-doping has attracted the interest of most researchers. F ions have been demonstrated to favor the incorporation of N ions into the TiO₂ crystal lattice, create oxygen vacancies [12a,b] and induce formation of Ti³⁺ ions [13]. As a result, N–F–TiO₂ catalysts exhibit higher absorption in the visible region and higher catalytic activity than N doped TiO₂ [12,13].

N–I co-doping has been explored to a lesser extend so far. To the best of our knowledge, only the study of Zhou et al. [16] reported the preparation of N–I co-doped TiO₂ in anatase phase via a hydrolysis method. According to the above study, some N atoms had replaced O atoms in the TiO₂ lattice and iodine existed in I⁷⁺, I⁵⁺ and I[−] oxidation states. N–I–TiO₂ catalysts showed higher photocatalytic

* Corresponding author. Tel.: +30 26410 74186; fax: +30 26410 74176.

E-mail address: iokonst@cc.uoi.gr (I. Konstantinou).

degradation of methyl orange (MO) compared with TiO₂ P25, N-doped and I-doped TiO₂ [16]. However the nature of the active centers and the mechanism of this improved photocatalytic activity has to be mapped out.

So far, in most cases, non-metal mono doped and co-doped TiO₂ materials have been used as oxidation photocatalysts. Wang et al. [12c] have reported the preparation of N–F co-doped TiO₂ and by theoretical calculations and experiments, they have shown that the co-doped materials could be used for efficient catalytic reduction of metal cations such Cr(VI), Ag(I) and Fe(III). Recently, the interest of researchers on the reduction of Cr(VI) in aqueous systems by TiO₂ catalysts has been increased [18]. In addition, EPR spectroscopy [19,20] has been proven a key-method for studying the photoactive paramagnetic species formed in such co-doped TiO₂ catalysts. In our recent report [21] we have successfully prepared N-doped and N–F co-doped TiO₂ which showed high photocatalytic efficiency for the reduction of Cr(VI) in the presence of oxalate ions. EPR spectroscopy provided key-information which allowed in-depth explanation for the catalytic performance of the co-doped TiO₂ materials. In addition, the most active N–F co-doped catalyst has been also studied for simultaneous Cr(VI) reduction and benzoic acid oxidation in aqueous solutions using an experimental design and response surface methodology for optimization of the experimental parameters [22].

As emanation of our previous reports [21,22] herein we investigate the physicochemical mechanism and the catalytic performance of N–I co-doped TiO₂ materials for the simultaneous oxidation of benzoic acid as organic pollutant and reduction of chromium (VI).

Cr(VI) and benzoic acid were selected as target compounds since they may be present in a great variety of industrial waste effluents and their simultaneous treatment will show both economic and technological profits [22]. Benzoic acid, the simplest aromatic carboxylic acid, is a model compound representative of the aromatic content typically found in various industrial wastewaters. Among heavy metals Cr(VI) is one of the most frequent and toxic contaminants in wastewaters arising from various industrial processes such as electroplating, pigment production, leather tanning, textile dying, wood preservation, as well as finishing of metals and plastics [18,22]. Finally, benzoic acid can act as hole and hydroxyl radical scavenger, inhibiting the recombination rate of photo-induced hole–electron pairs, thus increasing the Cr(VI) reduction ability of the prepared catalyst.

In the present work we have studied the preparation, via a sol gel method [21], and characterization of N–I co-doped TiO₂ materials. Their photocatalytic performance was evaluated for the simultaneous Cr(VI) reduction and benzoic acid oxidation. XRD analysis, and UV–vis absorption experiments were used for the characterization of crystal phase, size and light absorbance of catalysts. EPR spectroscopy was used for the detection of photoactive paramagnetic species in N–I co-doped TiO₂ solids and the study of the photo/redox mechanism.

2. Experimental

2.1. Preparation of materials

The preparation method was based on a sol–gel impregnation method as described previously [21] with some modifications. For the preparation of the N–I co-doped materials 3.4 mL titanium (IV) n-butoxide was added dropwise to 50 mL aqueous NH₄I solution at given concentrations under vigorous stirring. Four different concentrations of NH₄I solution were used to achieve final molar ratio of Ti to N–I [Ti/N–I] equal to 1, 3, 5 and 10. The obtained yellowish milky suspensions were aged for 24 h at room temperature and

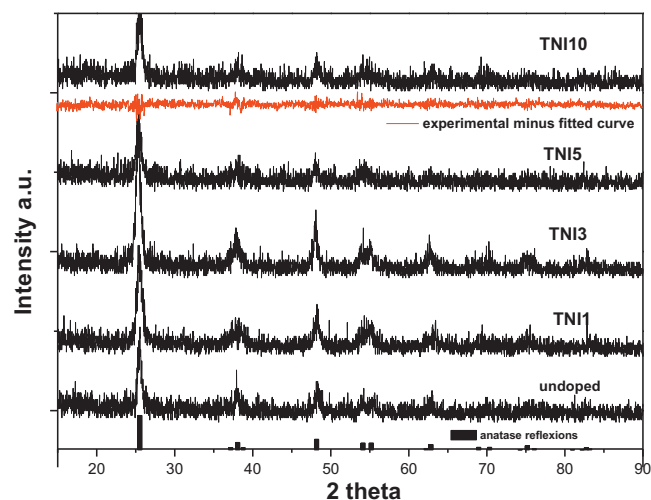


Fig. 1. Representative XRD patterns for all prepared N–I co-doped catalysts. The line plot above TNI10 sample represents difference plot between experimental and theoretical calculated (Rietveld analysis). Column type plot represents the reflections of TiO₂ anatase phase according to databank used.

subsequently dried at 100 °C for at least 48 h. The obtained xerogels were calcined at 500 °C in air for 1 h with a ramp rate of 5 °K/min. Afterwards, the calcined powders were dispersed in water and the suspensions were sonicated in a water sonication bath for 2 h and then washed with distilled water to remove impurities. Finally, the as-prepared catalysts were dried again at 110 °C and ground in agate mortar. In this way, we have prepared four N–I co-doped solids with Ti/N–I molar ratios of 1, 3, 5 and 10, herein named as TNI1, TNI3, TNI5 and TNI10, respectively. For comparison, undoped TiO₂ was also prepared by the same protocol.

2.2. XRD and surface area analysis

The crystal phases of all prepared N–I co-doped TiO₂ catalysts were characterized by recording their X-Ray Diffraction (XRD) patterns using a Brüker Advance D8 instrument employing Cu K radiation ($\lambda = 1.5418 \text{ \AA}$) in the 2θ range from 10° to 80° with a 2θ resolution of 0.02°. The XRD patterns were assigned using the Joint Committee on Powder Diffraction Standards (JCPDS) database and then were analyzed with Rietveld refinement using an applicable computer program.

Crystal size was calculated by the well-known Sheerer's equation: $d = 0.9\lambda / b \cos \theta$, where d is diameter of crystallites in nm, λ is the wavelength (nm) of the monochromatic X-ray beam, θ is the Bragg angle in degrees, and b is the FWHM. The results obtained from XRD analysis are presented in Fig. 1 and Table 1.

Nitrogen adsorption–desorption isotherms were determined at 77 K using a Tristar Micrometrics Instruments and the specific surface area of the N–I co-doped TiO₂ was derived using the Brunauer–Emmett–Teller (BET) method.

2.3. UV–vis–DRS measurements

The ultraviolet–visible diffuse reflectance spectra (UV–vis DRS) of the catalysts were measured by a Perkin Elmer (Lambda 35) spectrophotometer equipped with an integrating sphere assembly, using BaSO₄ as the reflectance standard, at room temperature, in the wavelength range 220–800 nm. The UV–vis DRS of all samples are shown in Fig. 2a. In Fig. 2b the compiled Kubelka–Munk plots [23] are presented.

Table 1
Results of XRD, Rietveld analysis and specific surface areas (BET) for the prepared N–I co-doped catalysts.

Code name	Crystal phase	XRD Rietveld analysis						Specific surface area BET (m ² /g)
		Space group	a	b	c	FWHM	Crystal size (nm)	
TiO ₂ databank phase	Anatase TiO ₂	Tetragonal I41	3.784	3.784	9.515			
Undoped TiO ₂	Anatase TiO ₂	Tetragonal I41	3.782	3.782	9.522	0.523	21	105
TNI-1	Anatase TiO ₂	Tetragonal I41	3.788	3.788	9.478	0.629	13	135
TNI-3	Anatase TiO ₂	Tetragonal I41	3.783	3.783	9.524	0.510	18	121
TNI-5	Anatase TiO ₂	Tetragonal I41	3.797	3.797	9.530	0.586	14	126
TNI-10	Anatase TiO ₂	Tetragonal I41	3.785	3.785	9.508	0.542	15	110

2.4. EPR experiments

Electron Paramagnetic Resonance (EPR) spectra were recorded with a Bruker ER200D spectrometer at liquid N₂ temperatures, equipped with an Agilent 5310A frequency counter. Adequate signal to noise was obtained after 5–10 scans. The spectrometer was running under home-made software based on Lab View [24a]. Spin quantitation was done using DPPH as spin standard [24b].

The effect of light irradiation on EPR spectra of the TiO₂ catalysts was investigated directly irradiating the sample into the EPR cavity using a 450 W solar-light source (Oriol model 66929, 290 < λ < 900 nm with a water IR cut-off filter).

For the investigation of the photoinduced formation of O₂^{•−} radicals on the surface of the catalysts under O₂ atmosphere and light conditions, the EPR tube with the TiO₂ catalyst was irradiated at room temperature for 10 min and then rapidly (<5 s) frozen in T = 77 K in the presence of ambient O₂. To detect the holes of tested

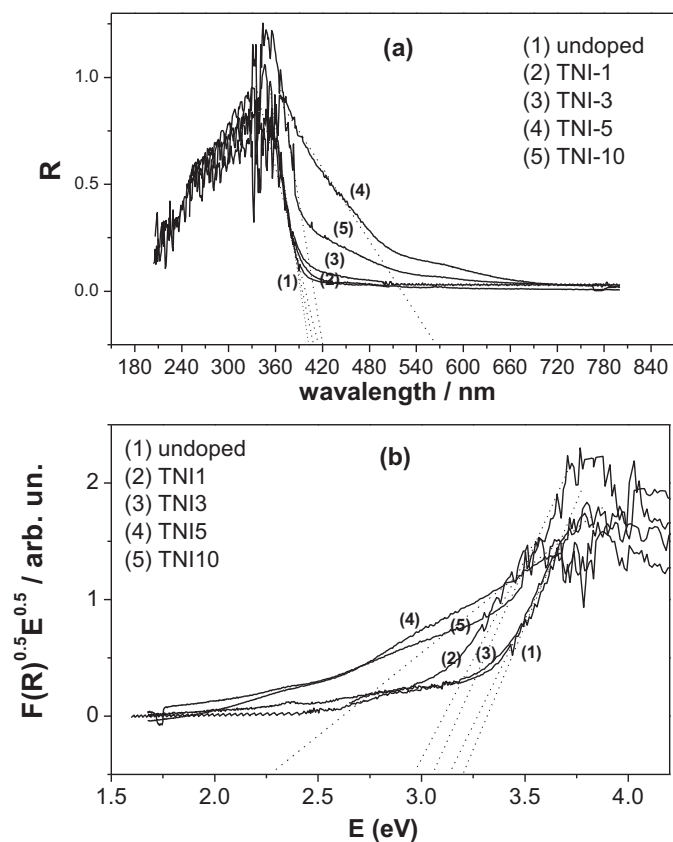


Fig. 2. (a) DR UV–vis spectra plots; (b) Kubelka–Munk plots of undoped TiO₂ and all N–I co-doped prepared solids. R: absorbance; $E = 1241.436/\lambda$: energy in eV, λ = wavelength in nm.

N–I co-doped TiO₂ samples, EPR illumination experiments with the use of isopropanol, as hole scavenger [25], were performed. The results of the EPR experiments are represented in Figs. 3–6 and Table 2.

Spin-lattice relaxation experiments [21,26] were performed in all N–I co-doped samples in order to correlate the catalytic behavior of the catalysts with the paramagnetic species. Progressive microwave saturation can be used to determine relative spin relaxation rates [26] in continuous wave EPR. The saturation curve is constructed by plotting the ratio of the signal amplitude to the square root of power vs. the incident microwave power [21,26]. The

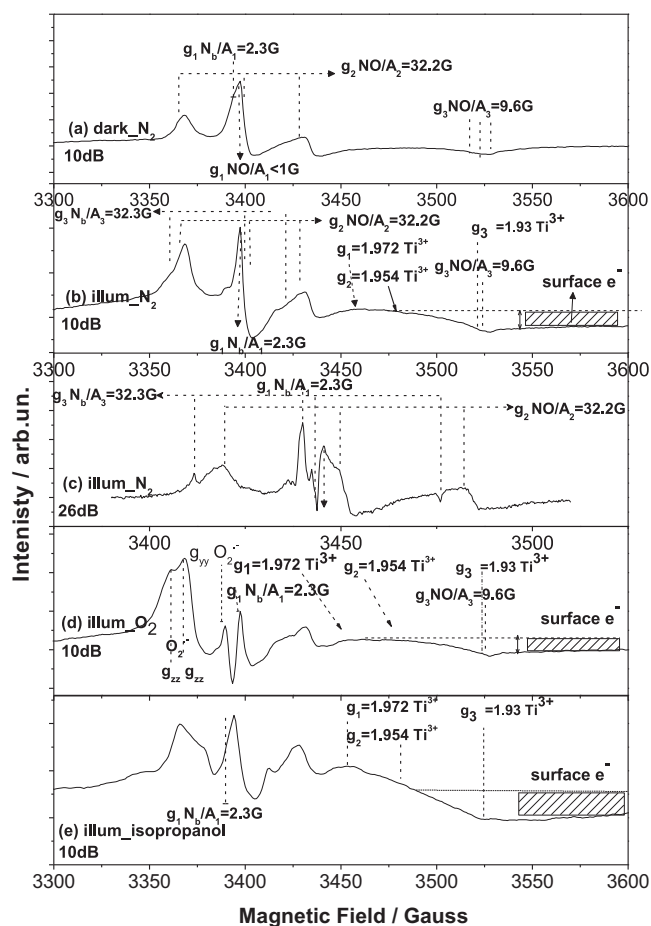


Fig. 3. Representative EPR spectra of the samples with code names TNI3. (a) At 77 K under dark; (b and c) illumination conditions at 77 K under N₂ atmosphere; (d) illumination conditions at 77 K under O₂ atmosphere; (e) illumination conditions at 77 K with isopropanol used as hole scavenger. Typical experimental conditions (a, b, d, e): amplifier, 1.552 mV; microwave power, 10 dB; sensitivity, 20 mV; time constant, 100 ms; (c): amplifier, 0.662 mV; microwave power, 26 dB; sensitivity, 20 mV; time constant, 100 ms.

Table 2

g- and ^{14}N ($I=1$) hyperfine-tensors of observed paramagnetic species in N-I co-doped TiO_2 prepared with different N-I ratios. With bold font are emphasized the g contents detected in N doped and N-I co-doped samples.

Paramagnetic species<	g_1	g_2	g_3	A_1/G	A_2/G	A_3/G	Reference
NO	2.001	1.998	1.927	<1	32.2	9.6	[29]
N_b^\bullet	2.005	2.004	2.003	2.3	4.4	32.3	[29]
Ti^{3+} lattice	1.990	1.964	1.940			1.99 1.964 1.94	[27]
Paramagnetic species	g_1	g_2	g_3	A_1/G	A_2/G	A_3/G	Reference
Ti^{3+} surface	1.972	1.954	1.930				[30,33]
Paramagnetic species	g_{zz}	g_{yy}	g_{xx}	A_1/G	A_2/G	A_3/G	Reference
$\text{O}_2^{\bullet-}$ [I]	2.0210	2.0090	2.0030				[33]
$\text{O}_2^{\bullet-}$ [II]	2.0184	2.0096	2.0033				[32]
$\text{TiO}^{4+}-\text{O}^{\bullet-}$	2.0046	2.0121	2.0121				[32]

saturation data are fit to the expression $I(P) = (1 + P/P_{1/2})^{-b/2}$ where I is the normalized EPR amplitude divided by the square root of the incident microwave power (P), $P_{1/2}$, the power at which the signal attains half of its unsaturated value and b the inhomogeneity parameter, are the two fitting parameters. Representative curves of $P_{1/2}$ experiment for TNF1 and TN1 samples are included in Fig. 7. The calculated values of $P_{1/2}$ for all N-I co-doped samples are presented in Table 3.

2.5. Photocatalytic experiments of simultaneous Cr(VI) reduction and benzoic acid oxidation

Photocatalytic experiments were carried out in a solar simulator Suntest XLS+ (Atlas, Germany) equipped with a 2.2 kW xenon lamp. The light source was jacked with special glass filters restricting the

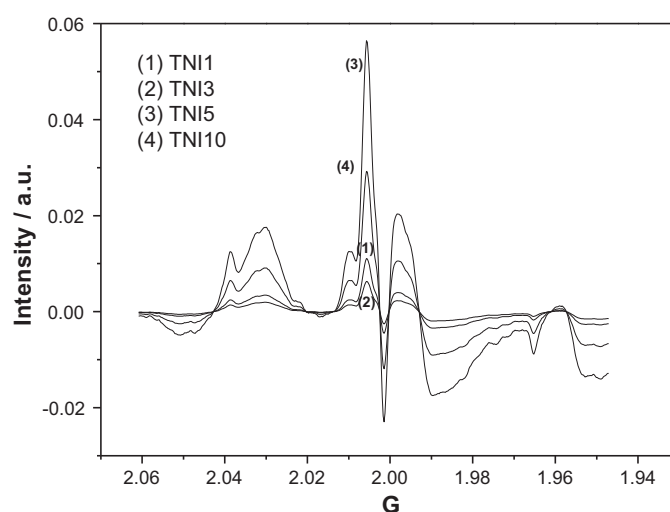


Fig. 5. EPR spectra for all N-I co-doped prepared materials with illumination conditions at 77 K under N_2 atmosphere for the reclusion of N_b^\bullet paramagnetic species.

transmission of wavelengths below 290 nm. The temperature of the samples was maintained at 25°C using a tap water cooling circuit preventing any heating of the suspension.

An average irradiation intensity of 600 W m^{-2} was maintained throughout the experiments and was measured by internal

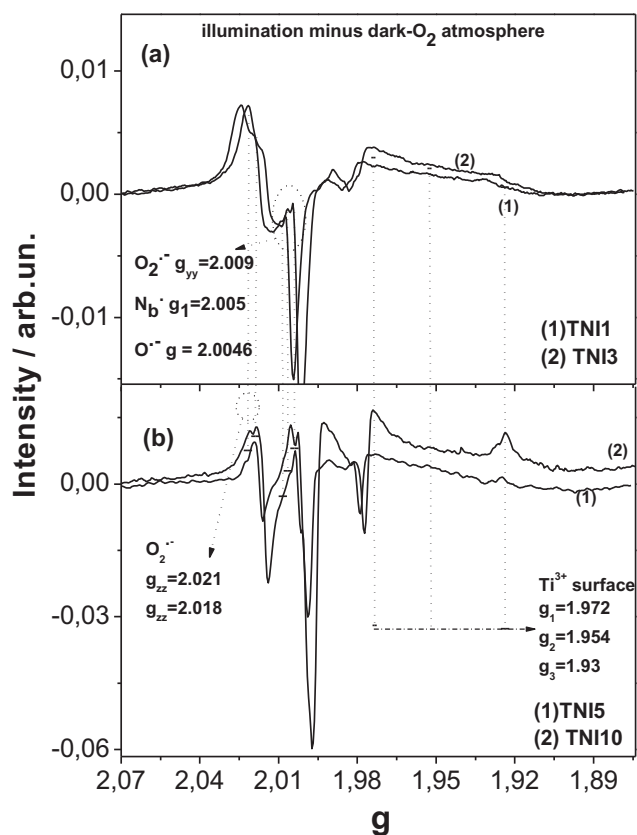


Fig. 4. Illumination minus dark plots for (a) TNI1, TNI3 samples and (b) TNI5, TNI10 samples.

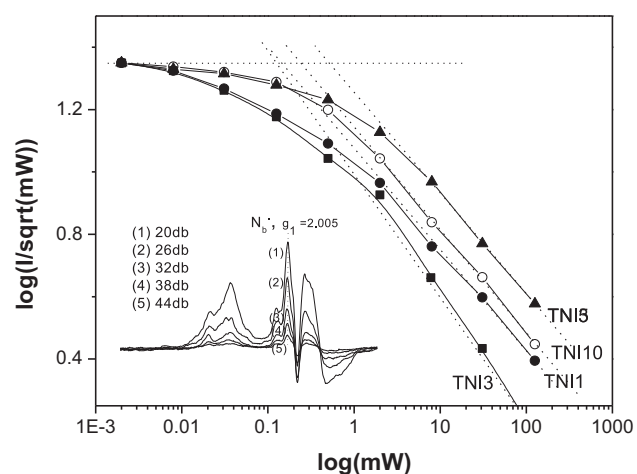


Fig. 6. Spin lattice relaxation plots for N_b^\bullet species at all N-I co-doped prepared catalysts. The attenuation of N_b^\bullet signal at 20, 26, 32, 38 and 44 dB is presented in the inset graph.

Table 3
 k_1^{BA} , k_1^{Cr} kinetic constants for benzoic acid oxidation, and Cr(VI) reduction, in comparison with all relevant characteristics studied in this report that could affect the photocatalytic reduction and/or oxidation rates such as crystallite size, E_g values, $P_{1/2}$ values and relative EPR signal intensities of photogenerated N_b^{\bullet} species, Ti^{3+} surface ions and $TiO^{4+}-O^{\bullet-}$ trapped holes detected by EPR.

Catalyst code name	k_1^{BA} oxidation	$k_1^{Cr(VI)}$ reduction	Crystallite size (nm)	$P_{1/2}$ log(mW)	E_g (eV)	I_{N_b} (N_b -photogeneration)	$I_{O^{\bullet-}}$ ($O^{\bullet-}$ radical photogeneration)	$I_{Ti^{3+}}$ surface (Ti^{3+} surface photogeneration)
TNI-1	125×10^{-4}	441×10^{-4}	13	0.25	2.97	12×10^{-3}	$\approx 18 \times 10^{-4}$	61×10^{-4}
TNI-3	120×10^{-4}	428×10^{-4}	18	0.13	3.11	7×10^{-3}	$\approx 16 \times 10^{-4}$	41×10^{-4}
TNI-5	80×10^{-4}	1706×10^{-4}	14	0.35	2.34	71×10^{-3}	122×10^{-4}	90×10^{-4}
TNI-10	96×10^{-4}	651×10^{-4}	15	0.32	2.91	31×10^{-3}	78×10^{-4}	283×10^{-4}
P25	205×10^{-4}	1070×10^{-4}	–	–	–	–	–	–
Undoped TiO_2	77×10^{-4}	411×10^{-4}	21	–	3.18	–	–	–

radiometer supplied by the manufacturer. Irradiation experiments were performed using a 250 mL Pyrex glass UV-reactor containing 250 mL of aqueous solutions at different pH values. The pH of solutions was adjusted by H_2SO_4 or NaOH aqueous solutions. The solutions were mixed with the appropriate amount of catalyst and were magnetically stirred before and during the illumination. The suspensions were kept in the dark for 30 min, prior to illumination in order to reach adsorption equilibrium onto semiconductor surface. As the reaction progressed, samples were withdrawn from the reactor at specific time intervals for further analysis.

Benzoic acid concentrations were determined by a Dionex P680 HPLC chromatography equipped with a Dionex PDA-100 Photodiode Array Detector using a Discovery C18 (250 mm length \times 4.6 mm ID; 5 μ m particle size) analytical column from Supelco (Bellefonte, PA, USA). The HPLC mobile phase was a mixture of LC-grade water H_2O (70%) pH 3 (adjusted with formic acid) and acetonitrile (30%) with a flow rate of 1 mL/min. Column temperature was set at 40 °C. The detection of benzoic acid was realized at 228 nm. The concentration of Cr(VI) was determined by the diphenylcarbazide colorimetric method [27] at a wavelength of 540 nm using a UV–Vis spectrophotometer (Hitachi, U-2000).

3. Results and discussion

3.1. XRD and surface area analysis

X-ray diffractograms for all prepared N–I co-doped catalysts are shown in Fig. 1. The reflections of TiO_2 anatase phase with space group tetragonal I41, as observed from the databank (JCPDS), are included in the bottom of Fig. 1 by the bar-diagram. Using the obtained phase for each solid as starting model, a Rietveld refinement of the obtained XRD data was made based on the methodology developed elsewhere [28]. In Fig. 1 the red line below TNI10 sample represents the difference between the experimental and theoretical pattern calculated from Rietveld refinement for TNI10 sample. The calculated refinement parameters including the cell parameters (a , b , c), FWHM (observed peak width at half maximum peak height in rads) and crystallite size, are included in Table 1. The average grain size is calculated using Scherrer's equation [28] based on the FWHM of the peak (1 0 1) of anatase.

The cell parameters in Table 1 for all prepared catalysts show small differences vs. the TiO_2 anatase phase values (JCPDS). These differences are in the expected range for this type of doping [12–16].

Crystal lattice distortion is reported to be important for absorption edge shift toward the visible-light region [12b]. In addition, the crystallite size of the catalysts is also important for the photocatalytic efficiency. N–I TiO_2 materials showed small crystal sizes (Table 1) in the range of $d_{XRD} = 13–18$ nm while for the undoped TiO_2 sample the crystal size was 21 nm.

In conclusion, the XRD data show that co-doping with N and I ions results to TiO_2 solids with some distortion of crystal lattice and low crystal size. This result is consistent with literature data reporting that dopants can favor formation of small particles [12–16]. For example, Zhou et al. [16] reported smaller particle sizes for N–I co-doped TiO_2 , e.g. 10.9 nm compared to undoped TiO_2 (15.8 nm). Nitrogen adsorption–desorption isotherms were determined at 77 K and the specific surface area was derived using the Brunauer–Emmett–Teller (BET) method. The measured N_2 -BET specific surface area of N–I co-doped TiO_2 catalysts were 135, 121, 126 and 110 m^2/g for TNI1, TNI3, TNI5 and TNI10, respectively (see Table 1). Thus, doping did not appreciably affect the surface area of the TiO_2 and the results can be related to the differences observed among the N–I TiO_2 samples in terms of anatase crystallite size since samples with the higher surface areas are composed of smaller TiO_2 particles.

3.2. UV–vis spectra

The UV–vis DRS of the prepared materials are presented in Fig. 2a. Pure TiO_2 is not able to respond to visible light, whereas TNI1 and TNI3 samples exhibited an extension of visible light absorption at 450 nm for TNI3 and 480 nm for TNI1 (see Fig. 2a). A higher visible light absorption was observed in the case of TNI10 sample

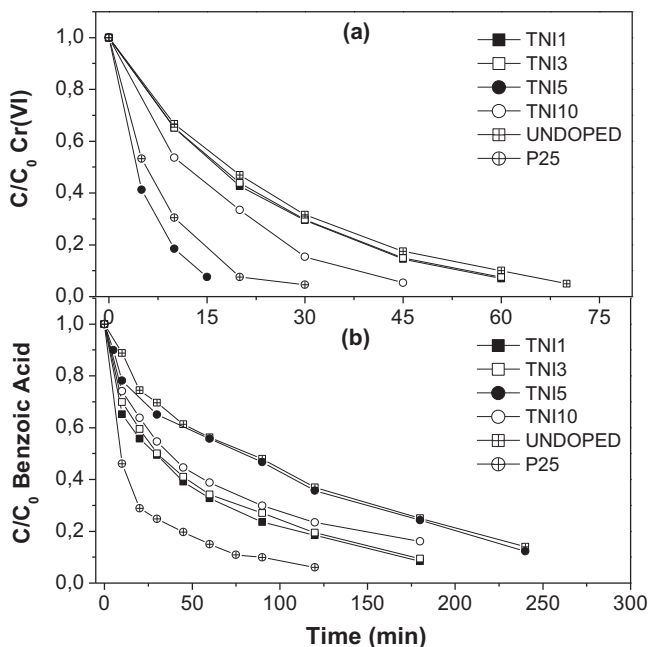


Fig. 7. Time profile of (a) Cr(VI) reduction and (b) benzoic acid oxidation using 500 ppm catalyst suspensions at pH 2, under air conditions for all N–I co-doped prepared catalysts in comparison with undoped TiO_2 sample and Degussa P25. Initial concentrations of Cr(VI) = 0.05 mM and benzoic acid = 0.01 mM.

which started at around 600 nm while the highest absorption was observed in the case of TNI5 sample starting from 680 nm.

Band-gap energies, E_g , for the as-prepared N-I-co-doped TiO₂ photocatalysts were calculated by plotting the transformed Kubelka–Munk function vs. energy [23] as shown in Fig. 2b. The calculated E_g values are listed in Table 3. E_g values of 2.97, 3.11 and 2.91 eV were determined for TNI1, TNI3 and TNI10, respectively. TNI5 had the most significant visible light absorption with a band gap of 2.34 eV.

The E_g values of TNI1, TNI3 and TNI10 were comparable to E_g band gaps obtained for N-doped and N-F co-doped TiO₂ in our previous study [21] and they are associated to the impurity states deriving from N-insertion in the bulk of the oxide. The E_g value of TNI5 sample is comparable to that previously reported in the literature for N-I doped TiO₂ [16]. As reported previously [20], inserted N ions can either substitute lattice oxygen or be bound interstitially with lattice oxygen to form two types of N-based paramagnetic moieties, i.e. named N_b^\bullet (b = bulk), in the bulk of the solid. These N_b^\bullet paramagnetic species are clearly detectable with EPR spectroscopy, as will be also shown in the next section. These N-states are located ~0.7–0.8 eV above the valence band (VB) and are responsible of the optical absorption in the visible range of such N doped TiO₂ solids [20]. With regard to the iodine doping, according to Su et al. [29] the possible iodine species (I^{7+} , I^{5+} , I^-) can be incorporated on the surface of anatase particles. This can introduce an interband energy level ~–0.5 eV below the E_{VB} of anatase which it turn can account for a sub-band-gap transition mechanism corresponding the visible light photoactivity [29].

3.3. EPR characterization of paramagnetic species

Typical EPR spectra for TNI3 sample in the dark are shown in Fig. 3a. The g- and ¹⁴N ($I = 1$) hyperfine-tensors for all paramagnetic species observed by EPR are reported in Table 2. Using these g- and A-tensors, the structural assignment of these centers was done according to previous reports [30,31]. For reference, the values reported by Giamello's group [30] and Ahn et al. [31b] are also included in Table 2.

The EPR spectra shown in Fig. 3a depict the assignment of NO centers based on the g-values and lineshapes [30]. The dashed bars mark the g- and ¹⁴N-tensors of the NO centers.

In Fig. 3a, the g_1 (2.001), g_2 (1.998), g_3 (1.927) [30] components of NO species can be resolved with a ¹⁴N-hyperfine splitting <1 G, 32.2 G and 9.6 G, respectively. It is also denoted the weak signal of g_1 (2.005) component of N_b^\bullet [30,31a] species which is overwhelmed by the stronger g_1 (2.001) component of NO centers.

The EPR signal of TNI3 sample under illumination in N₂ atmosphere is presented in Fig. 3b. It is observed that under illumination the NO signals get weaker, while the N_b^\bullet signals increased. As a result, under illumination in N₂ atmosphere, the g_1 (2.005) component of N_b^\bullet species is clearly resolved while the g_2 (1.998) of NO centers is attenuated. This phenomenon has been observed also in our previous report [21] and agrees with the fact that the NO center is non-photoactive, it is trapped in microvoids of the solid and is detected by EPR when adsorbed on the surface [30a]. The more interesting photoinduced N_b^\bullet species [30b] are localized deeper in the lattice of TiO₂ solids. They are based either on a substitutional nitrogen (N substitutes O in some lattice position) or on interstitial N that is chemically bound to a lattice oxygen ion thus, forming a sort of NO group in the bulk of the solid [20]. A fraction of these centers bear one electron in the singly occupied molecular orbital and is consequently paramagnetic and EPR active. Napoli et al. [31a] combined EPR and XPS measurements to indicate that such interstitial bound N_b^\bullet species can be described in chemical terms as an ion. The energy levels of these N_b^\bullet species are placed well below those of Ti^{3+} states [31].

In addition, in Fig. 3b photoinduced signals of Ti^{3+} ions were detected. The broad signals with $g_1 = 1.972$ and $g_2 = 1.954$ correspond to Ti^{3+} ions formed on the surface [31b]. Rajh et al. [32] reported that the broad nature of Ti^{3+} surface ions signal is indicative of a wide distribution of surface sites with differing geometries and therefore varying trapping energies. The formation of Ti^{3+} surface ions is reported [8–10] to be correlated with iodine dopant dosage. Zhang et al. [8b] stated that I^{5+} substitutes Ti^{4+} in the lattice and Ti^{3+} are generated to balance the charge. Thus the percentage of Ti^{3+}/Ti^{4+} increased in correlation with the nominal by weight iodine concentration. Similar results were also presented by Zhou et al. [16] for co-doped N-I catalysts.

In Fig. 3c the EPR spectra of TNI3 recorded at low microwave power is shown. Under these EPR conditions the observation of N_b^\bullet species is easier, due to attenuation of the signal by weakly physisorbed NO centers [30]. Thus, in Fig. 3c the g_1 (2.005) component of N_b^\bullet or (NO^{2-}) species is more apparent and the g_3 (2.003) component – with a 32.3 G ¹⁴N-hyperfine splitting – can be better resolved.

In order to elucidate the effect of O₂ on trapped electrons, the TNI3 sample was illuminated under O₂ (Fig. 3d). In this spectrum, the g_{zz} components of two types of $O_2^{\bullet-}$ radicals, at 2.021 and 2.0184 [33] partially overlap with the NO signal. The g_{yy} component of $O_2^{\bullet-}$ at 2.0096 is also resolved at the left side of g_1 (2.005) component of N_b^\bullet species. The associated g values are assigned to adsorbed superoxy species $O_2^{\bullet-}$ [33,34]. In EPR studies dealing with the investigation of oxide surfaces, this type of oxygen radical is widely used as a probe for cationic surface sites because it has specific resonances within the low field region (g_{zz}) which are indicative of the local crystal fields at the respective $O_2^{\bullet-}$ adsorption sites [33]. In the present case, two different surface cations could serve as adsorption sites for the formed oxygen radicals as evidenced by their resonances at $g_{zz} = 2.021$ and $g_{zz} = 2.018$. The first type with $g = 2.021$ assigned to $Ti^{4+}-O_2^{\bullet-}$ bonds on anatase, formed after TiO₂ reduction or UV irradiation and requires O₂ adsorption [34]. The second type with $g = 2.0184$ was probably produced by Ti^{3+} surface ions.

Finally, the EPR signals of TNI3 obtained in the presence of isopropanol as positive hole (h^+) scavenger are shown in Fig. 3e. It is observed that the signal of N_b^\bullet species disappeared, a fact also established in previous reports [21,30] which means that such species react as positive holes in the doped TiO₂ catalysts. In addition, an increase of Ti^{3+} ions is observed at $g = 1.954$ and $g = 1.93$.

To summarize, the present EPR experiments showed: [i] the formation of weakly physisorbed NO paramagnetic centers and lattice N_b^\bullet or (NO^{2-}) paramagnetic species localized deeper in the solid lattice, which act as positive holes; [ii] the detection of surface Ti^{3+} ions with $g_1 = 1.972$ and $g_2 = 1.954$; [iii] the formation of two types of $O_2^{\bullet-}$ radicals upon illumination under O₂ atmosphere.

Illumination-minus-dark plots (Fig. 4) allow better anticipation of the photogenerated species.

In Fig. 4, the formation of $O_2^{\bullet-}$ radicals, N_b^\bullet species and Ti^{3+} lattice and surface ions is clearly viewed. In addition, the photo-generation of the axial signal $g_{||} = 2.0046$ (see Table 2) assigned to $TiO^{4+}-O^{\bullet-}$ trapped holes [33] which is too close to the $g_1 = 2.005$ signal of N_b^\bullet species can also be resolved. According to Berger et al. [33] these trapped holes were produced from the reaction of anatase holes with the lattice oxygen ions O^{2-} . At a first glance, less N_b^\bullet and $TiO^{4+}-O^{\bullet-}$ hole signals were obtained in TNI1 and TNI3 samples (Fig. 4a) in comparison with the TNI5 and TNI10 samples (Fig. 4b).

In addition, the intensities of $O_2^{\bullet-}$ radicals, N_b^\bullet species, $TiO^{4+}-O^{\bullet-}$ holes and Ti^{3+} surface ions, follow the series: TNI3 < TNI1 < TNI5 < TNI10. The illumination-minus-dark EPR spectra for all samples under low microwave power are presented in Fig. 5.

N_b^\bullet species are better resolved, i.e. without interference from the $TiO^{4+}-O^{\bullet-}$ hole signals. Based on the intensity of the central component ($g=2.005$) ($I_{N_b^\bullet}$) we conclude that the relative concentration of formed N_b^\bullet photoexcited species also follows the series: $TNI3 < TNI1 < TNI5 < TNI10$.

The relative intensities of N_b^\bullet species, $TiO^{4+}-O^{\bullet-}$ holes and Ti^{3+} surface ions denoted as $I_{N_b^\bullet}$, $I_{O^{\bullet-}}$ and $I_{Ti^{3+} \text{ surface}}$ are summarized in Table 3, and will be used to discuss the photocatalytic activity of the catalysts in conjunction with the photoexcited species detected by EPR. The intensities of $O_2^{\bullet-}$ radicals cannot be used for quantitative analysis due to their overlap by the NO signals.

3.4. Microwave EPR saturation study for the N_b^\bullet centers

The progressive saturation data for the $g_1=2.005$ signal at 77 K are displayed in Fig. 6 for all catalysts. The signal saturated easily with no changes in the line-shape.

The microwave saturation values $P_{1/2}$ for the N_b^\bullet centers of the catalysts are listed in Table 3. To better understand the significance of these numbers we briefly reiterate the basic underlying mechanism which results in shifts of the $P_{1/2}$ values. For $S=1/2$ systems like the ones studied herein for the TiO_2 materials, spin lattice coupling is the main mechanism which determines the $P_{1/2}$ values.

This spin-lattice coupling is mediated by the g -tensor and the A -tensor [35,36]. Thus, an increase of the $P_{1/2}$ value for comparable $S=1/2$ systems, e.g. N_b^\bullet or $(NO_2)^-$ species in the various N–I catalysts, reflects an enhanced spin-lattice coupling. This can be the result of [i] stronger N–O bonds, [ii] the positioning of the N_b^\bullet centers deeper in the crystal. Stronger N–O bond will be manifested as shifts in g -values, which is not the case for our samples (see Table 3). Thus, the higher $P_{1/2}$ values for the N_b^\bullet centers can be attributed to the localization of N_b^\bullet centers deeper into the crystal sites [21]. More precisely, the $P_{1/2}$ values of the N_b^\bullet centers followed the sequence: $TNI5 > TNI10 > TNI1 > TNI3$. This result is correlated with the E_g values see Table 3. In previous reports [12,13,21] it was shown that light absorption of N-doped TiO_2 catalysts is proportional to the degree of N_b^\bullet species insertion in the TiO_2 lattice. In the present study the TNI5 and TNI10 catalysts, where N_b^\bullet species were found deeper in the lattice of TiO_2 , have the lowest E_g values (2.34 and 2.91 eV, respectively) in comparison with E_g values of TNI1 and TNI3 (2.97 and 3.11 eV, respectively).

3.5. Photocatalytic experiments of simultaneous Cr(VI) reduction and benzoic acid oxidation

Before photocatalytic experiments, the adsorption of Cr(VI) and benzoic acid in the prepared catalysts was measured after 30 min of stirring in darkness. The adsorption of Cr(VI) was 4%, 13.0%, 13.4%, 15.6% and 9.0% for the undoped- TiO_2 , TNI1, TNI3, TNI5 and TNI10 catalysts, respectively. Lower percentages were measured for benzoic acid; i.e. 2%, 6.4%, 4.0%, 6.0% and 6.0% for the undoped- TiO_2 , TNI1, TNI3, TNI5 and TNI10 catalysts, respectively. Fig. 7 shows the kinetic profiles for the simultaneous Cr(VI) reduction (Fig. 7a) and benzoic acid oxidation (Fig. 7b), at pH = 2 for all prepared N–I co-doped TiO_2 catalysts. The kinetic profiles of undoped TiO_2 and Degussa-P25 catalysts are also shown for comparison.

The first-order kinetic constants k_1^{Cr} , k_1^{BA} for BA oxidation and Cr(VI) reduction respectively, are listed in Table 3.

According to the kinetic data, all N–I co-doped catalysts studied herein presented higher reduction and oxidations rates compared to the undoped TiO_2 . In addition it is observed that the N–I co-doped catalysts perform faster the Cr(VI) reduction than BA oxidation. TNI5 presented the higher reduction activity, even from P25- TiO_2 , while P25 remains the most active oxidation catalyst (Fig. 7). Also, it must be underlined that in the case of P25 the concentration of

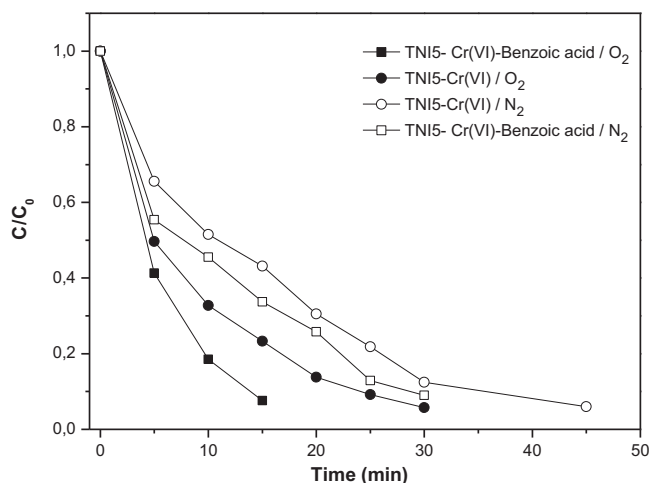


Fig. 8. Comparative time profiles of Cr(VI) reduction in the presence or absence of benzoic acid ions and under O_2 or N_2 atmosphere.

Cr(VI) started to increase after 90 min irradiation, probably because of the re-oxidation of Cr(III) ions caused by positive holes (h^+).

Overall, the activity toward photocatalytic Cr(VI) reduction followed the sequence: $TNI5 > P25 > TNI10 > TNI1 > TNI3 \geq$ undoped TiO_2 , while the photocatalytic oxidation activity the sequence: $P25 > TNI3 > TNI1 > TNI10 > TNI5 \geq$ undoped TiO_2 . The differences in reduction vs. oxidation activity will be explained further down in combination with EPR results.

In order to get more information on the role of O_2 in the photo/redox mechanism, additional photocatalytic runs were performed in N_2 atmosphere for the more active reduction catalyst, TNI5. The photocatalytic kinetics for Cr(VI) reduction in the presence and absence of benzoic acid, under O_2 or N_2 atmosphere are compared in Fig. 8.

As can be seen from Fig. 8, benzoic acid under N_2 atmosphere accelerates the reduction rates of Cr(VI). Moreover the presence of O_2 appears to promote the reduction of Cr(VI). These data indicate that: [i] benzoic acid acts as hole scavenger [8c] inhibiting the recombination of hole–electron pairs, accelerating thus the reduction ability of TNI5, and [ii] O_2 molecules seems to play a special role in the redox mechanism of such catalysts.

Table 3 summarizes all the relevant characteristics of the N–I catalysts that could affect the photocatalytic reduction and/or oxidation rates. The k_1^{BA} values for benzoic acid oxidation, follow the sequence $TNI5 < TNI10 < TNI1 < TNI3$ while the k_1^{Cr} values for Cr(VI) reduction are higher for TNI5 sample and lower for TNI3. Taking into consideration the crystallite size of all N–I co-doped catalysts that range from 13 to 18 nm, and the above catalytic trends no obvious correlation can be suggested. On the other hand, a correlation between E_g and the reduction rates of N–I co-doped catalysts is evidenced from Table 3. However such a correlation does not seem to hold between E_g and oxidation rates. Thus, E_g and crystallite size values alone cannot explain the observed reduction and oxidation rates.

A close inspection of the data in Table 3 suggests that, the key factors for the explanation of simultaneous Cr(VI) reduction and benzoic acid oxidation are the detected photogenerated species N_b^\bullet , $TiO^{4+}-O^{\bullet-}$ and Ti^{3+} .

Let us summarize the EPR data which pertain to key-characteristics for the prepared N–I catalysts. [i] All TiO_2 catalysts bear characteristic N-based paramagnetic centers i.e. the non-photoactive – weakly physisorbed molecular NO species, and highly photoactive lattice N_b^\bullet species, [ii] surface Ti^{3+} ions, [iii] adsorbed $O_2^{\bullet-}$ radicals were also detected in all N–I co-doped

materials and [iv] strong signals from $\text{TiO}^{4+}-\text{O}^{\bullet-}$ holes were detected in the case of TNI5 and TNI10, while in TNI1 and TNI3 the $\text{Ti}^{4+}-\text{O}^{\bullet-}$ holes signals were barely observed. In other words, N_b^{\bullet} species and surface Ti^{3+} ions seem to be the main photoinduced species while $\text{O}_2^{\bullet-}$ radicals and $\text{Ti}^{4+}-\text{O}^{\bullet-}$ holes represent photo-generated scavenged electrons and trapped holes, respectively. In this context, in the following section we analyze further the role of N_b^{\bullet} species and Ti^{3+} ions in the redox mechanism.

3.5.1. On the role of N_b^{\bullet} species

The photogeneration of N_b^{\bullet} species has been extensively studied by Giamello's group [20,30,37] and by our group for N-doped and N-F co-doped catalysts [21]. Accordingly, N_b^{\bullet} species increase the energy of the valence band E_{VB} level. These N_b^{\bullet} species can react as electron transfer centers via two different paths:

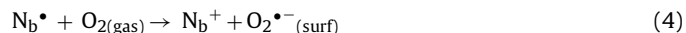
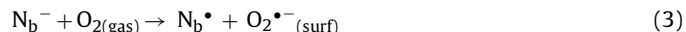
(A) When Ti^{3+} lattice ions are formed as observed in N-F co-doped TiO_2 in the previous study [21], an electron transfer occurs between N_b^{\bullet} and Ti^{3+} according to reaction (1):



(B) In the absence of lattice Ti^{3+} ions, electron transfer takes place under irradiation via the transformation of diamagnetic N_b^- species to paramagnetic N_b^{\bullet} [37] according to the following route (2):



Besides, as shown in previous reports [30,37], in the presence of O_2 , a fraction of photoexcited electrons is scavenged by O_2 , producing adsorbed $\text{O}_2^{\bullet-}$ through routes (3) and (4):



So, from the above mentioned reaction routes, it can be suggested that in the case of N-I co-doped solids where almost exclusively surface Ti^{3+} ions are produced, e.g. practically minimal or zero lattice Ti^{3+} , the interaction between Ti^{4+} and N_b^{\bullet} through reaction (1) is less possible. On the contrary, electron photogeneration takes place mainly through reaction (2). Also reactions (3) and (4) may be possible routes for the formation of the two types of observed $\text{O}_2^{\bullet-}$ signals.

The photogenerated electrons produced by the N_b^{\bullet} species can directly reduce Cr(VI) ions. This explains why reduction rates (k_1^{Cr} constant) are in direct correlation with the trend of N_b^{\bullet} species formation (see Table 3). This phenomenon has been also underlined in our previous report [21] where the Cr(VI) reduction in the presence of oxalate has been studied for N doped and N-F co-doped catalysts.

It must be also reminded that the concentration of the N_b^{\bullet} species defines the visible light absorption and it is correlated with E_g values which also followed the same trend with reduction rates (see Table 3). This result is more pronounced in Fig. 9 where E_g values, kinetic constants k_1^{BA} , $k_1^{\text{Cr(VI)}}$ and relative height of N_b^{\bullet} species signal ($I_{\text{N}_b^{\bullet}}$) are plotted for all N-I co-doped TiO_2 catalysts.

From Fig. 9 it is obvious that oxidation rates (k_1^{BA}) of all tested catalysts are quite the same and not affected by E_g , while reduction rates (k_1^{Cr}) have the same trend with $I_{\text{N}_b^{\bullet}}$ values and the inverse trend vs. E_g values.

3.5.2. The role of iodine ions

The presence of iodine ions can be beneficial for the photocatalytic reduction activity of N-I- TiO_2 catalysts. Using XPS, Zhou et al. [16] concluded that iodine ions can exist in I^{7+} , I^- and I^{5+} oxidation states in N-I TiO_2 catalysts. Moreover, they have observed that I^{7+} and I^{5+} can accept electrons excited from the valence band of TiO_2

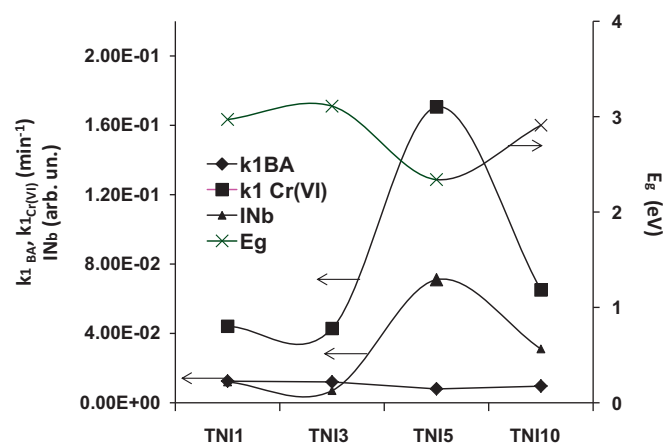
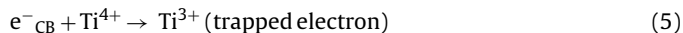


Fig. 9. Plots of calculated kinetic constants k_1^{BA} and k_1^{Cr} in comparison with E_g values and relative heights of photoexcited N_b^{\bullet} species ($I_{\text{N}_b^{\bullet}}$) for all tested N-I co-doped TiO_2 catalysts.

or N_b^- species while I^- can accept positive holes (h^+) preventing in this way electron-hole recombination [16]. So, capturing of electrons by I^{7+} or I^{5+} ions is another possible/supporting reduction route, particularly in the case of higher-iodine doping samples such as TNI5 and TNI10.

3.5.3. The role of surface Ti^{3+} states

Another crucial point is the role of Ti^{3+} ions; Berger et al. [33] reported that anatase Ti^{4+} ions can trap electrons to form surface Ti^{3+} ions through reaction (5):



Previous reports [20,31b,33] and the recent review of Xiong et al. [38] highlighted that surface Ti^{3+} defects improve the photocatalytic activity of TiO_2 due to: (i) extension of TiO_2 photoresponse from UV to visible light region, which leads to visible-light photocatalytic activity, (ii) reaction of surface sites with various adsorbates from the suspensions, resulting in the reduction of electron-hole pair recombination rate [38]. Thus, according to Xiong et al. [37] in the presence of O_2 , the Ti^{3+} surface sites easily react with O_2 , leading to the formation of radicals such as $\text{O}_2^{\bullet-}$, HO_2^{\bullet} , and OH^{\bullet} .

This type of charge transfer can be described by the following equations [38]:



As a conclusion, Ti^{3+} surface states can play a dual role: [i] charge transfer to adsorbed Cr(VI) or [ii] capturing of O_2 or other adsorbates, to form $\text{O}_2^{\bullet-}$ and HO_2^{\bullet} , OH^{\bullet} with subsequent reactions, inhibiting the recombination rate of electron-hole pairs. Thus, surface Ti^{3+} electrons can be consumed via various reaction paths not exclusively via Cr(VI) reduction. It must be also mentioned that Eq. (7) seems to be the more probable way for the formation of $\text{O}_2^{\bullet-}$ radicals that are detected by EPR herein.

Additional evidence for the key role of surface Ti^{3+} ions in the redox mechanism could be drawn by the experiments of Cr(VI) reduction (Fig. 8) that showed decreased reduction of Cr(VI) in the

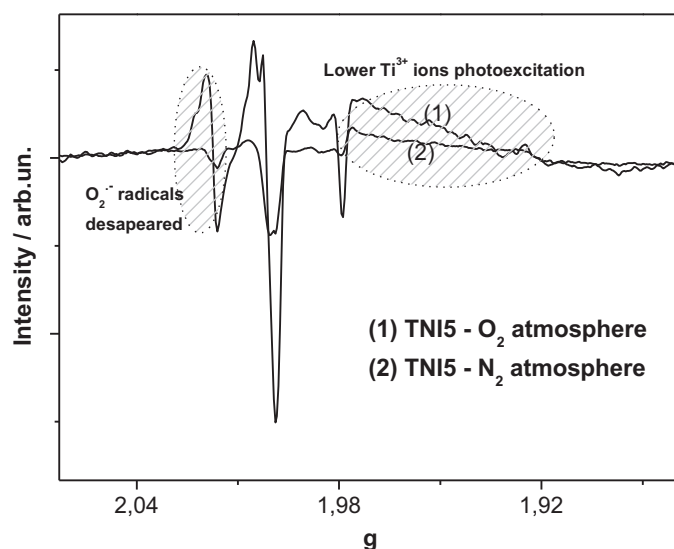


Fig. 10. Illumination minus dark EPR plots for TNI5 sample under O₂ and N₂ atmosphere for comparison.

absence of O₂ or benzoic acid, i.e. species that capture electrons or holes respectively, thus allowing electron–hole recombination. This result is also consistent with the EPR experiments presented in Fig. 10 showing the illumination-minus-dark signals of TNI5 under O₂ and N₂ atmosphere for comparison.

The photogeneration of surface Ti³⁺ ions in the absence of O₂, e.g. N₂ atmosphere, was decreased, while the O₂^{•−} radicals' signals disappeared. This fact proves that Ti³⁺ photogeneration take place through concurrent O₂ capturing.

3.5.4. On the role of TiO⁴⁺–O^{•−} holes

Finally the role of trapped holes TiO⁴⁺–O^{•−} will be discussed. According to previous reports [32–34,38] these trapped holes are produced from the reaction of holes (h⁺) of anatase phase with the lattice oxygen O^{2−} as follows:



Ross Macdonald et al. in their recent report [39] have also noticed that TiO⁴⁺–O^{•−} trapped hole EPR signals are barely detected or have much lower intensity than trapped electrons in anatase phase. In their view [39], the most plausible explanation for the absence of trapped holes is that on fully hydroxylated titania, surfacial VB holes react with surface OH groups to form hydroxyl radicals, which can oxidize organic molecules such as benzoic acid. It should be noted that benzoic acid is primary oxidized by •OH radicals according to [40].

In accordance with the previous statements, we suggest that the detection of higher intensities of EPR signals of trapped holes (Ti⁴⁺–O^{•−}), as in the case of TNI5 and TNI10 samples (see Fig. 5 and Table 3 I₀-values), indicates lower formation of •OH radicals, thus lower efficiency for benzoic acid degradation. When the detected trapped hole (TiO⁴⁺–O^{•−}) signals are absent as in the case of TNI1 and TNI3 (see Fig. 5 and Table 3 I₀-values) more •OH radicals were formed to oxidize benzoic acid. In other words, as the concentration of detected trapped holes increases, the number of free holes available for direct oxidation or •OH oxidation decreases. In accordance with our suggestion, Tojo et al. [10] studied the photooxidation mechanism of iodine-doped TiO₂ and suggested that the recombination of electron-hole pairs is inhibited because the doping I sites act as trapping e[−] sites. In addition, they reported that surface OH groups were significantly decreased by I-doping and that the trapped holes (h⁺) in I-TiO₂ have no significant oxidation

reactivity toward substrates, such as aliphatic and aromatic compounds, a fact that is consistent with the present results.

To summarize, the key-information of the study is that [i] the EPR intensity of detected paramagnetic N_b[•] species is in direct correlation with the formation of surface e[−] and thus the reduction ability of all N–I co-doped catalysts, while [ii] the detection of higher concentration of TiO⁴⁺–O^{•−} trapped holes, imply lower oxidation ability of such solids; [iii] surface Ti³⁺ ions in combination with the O₂^{•−} radicals support both reduction and oxidation mechanisms inhibiting electron–hole recombination.

4. Conclusions

N–I co-doped TiO₂ catalysts were successfully prepared via a sol–gel method. Anatase phase with tetragonal I41 space-group was formed in all cases while the crystal size of the prepared solids varied from 13 to 18 nm. In all cases N–I co-doping caused a band gap narrowing with E_g varying from 3.11 to 2.34 eV. Photocatalytic experiments for the simultaneous reduction of Cr(VI) ions and oxidation of benzoic acid showed a higher activity for all co-doped catalysts vs. the undoped TiO₂. EPR studies showed that N doping creates two kinds of nitrogen paramagnetic species: [i] non-photoactive NO centers, and [ii] highly photoexcited N_b[•] species which correlated with the photogenerated electrons through the path: N_b[−] → N_b[•] + e[−]. The location of N_b[•] species in the crystal lattice is correlated to E_g values as evidenced by EPR microwave saturation experiments. The Cr(VI)-reduction efficiency of N–I co-doped catalysts is correlated with the concentration of N_b[•] species and the E_g values. Doping with iodine ions, promotes formation of photoinduced surface Ti³⁺ electrons. Ti³⁺ surface ions can react [i] with the adsorbed Cr(VI), [ii] and/or O₂ to form radicals such as O₂^{•−}, HO₂^{•−}, and OH[•] supporting both reduction and oxidation mechanisms. Finally, EPR experiments showed the stabilization of oxygen trapped holes TiO⁴⁺–O^{•−} created by the reaction of anatase holes with lattice oxygen O^{2−}. The concentration of such stabilized trapped holes detected in the N–I catalysts is inversely correlated with the oxidation rates.

Acknowledgements

This research has been co-financed by the European Union (European Social Fund – ESF) and Greek National Funds through the Operational Program “Education and Lifelong Learning” of the National Strategic Reference Framework (NSRF) – Research Funding Program: THALIS. Investing in knowledge society through the European Social Fund.

References

- [1] M. Anpo, M. Takeuchi, *Journal of Catalysis* 216 (2003) 505–516.
- [2] I.K. Konstantinou, T.A. Albanis, *Applied Catalysis B: Environmental* 42 (2003) 319–335.
- [3] J.M. Wu, T.W. Zhang, *Journal of Photochemistry and Photobiology A: Chemistry* 162 (2004) 171–177.
- [4] J. Yuan, M.X. Chen, J.W. Shi, W.F. Shangguan, *International Journal of Hydrogen Energy* 31 (2006) 1326–1331.
- [5] C. Burda, Y.B. Lou, X.B. Chen, C.S. Samia, J. Stout, J.L. Gole, *Nano Letters* 3 (8) (2003) 1049–1051.
- [6] Y. Choi, T. Umehayashi, M. Yoshikawa, *Journal of Materials Science* 39 (2004) 1837–1839.
- [7] T. Ohno, M. Akiyoshi, T. Umehayashi, K. Asai, T. MitSui, M. Matsumura, *Applied Catalysis A: General* 265 (2004) 115–121.
- [8] (a) X. Hong, Z. Wang, W. Cai, F. Lu, J. Zhang, Y. Yang, N. Ma, Y. Liu, *Chemistry of Materials* 17 (2005) 1548–1552; (b) Q. Zhang, Y. Li, E.A. Ackerman, M. Gajdardziska-Josifovska, H. Li, *Applied Catalysis A: General* 400 (2011) 195–202.
- [9] V. Stengl, T.M. Grygar, *International Journal of Photoenergy* (2011) 13, <http://dx.doi.org/10.1155/2011/685935>, Article ID 685935.
- [10] S. Tojo, T. Tachikawa, M. Fujitsuka, T. Majima, *Journal of Physical Chemistry C* 112 (2008) 14948–14954.
- [11] J. Xu, Y. Ao, D. Fu, C. Yuan, *Applied Surface Science* 254 (2008) 3033–3038.

- [12] (a) D.-G. Huang, S.-J. Liao, J.-M. Liu, Z. Dang, L. Petrik, *Journal of Photochemistry and Photobiology A: Chemistry* 184 (2006) 282–288;
(b) Y. Xie, Y. Li, X. Zhao, *Journal of Molecular Catalysis A: Chemical* 277 (2007) 119–126;
(c) Q. Wang, C. Chen, W. Ma, H. Zhu, J. Zhao, *Chemistry – A European Journal* 15 (2009) 4765–4769.
- [13] (a) M. Pelaez, A.A. Cruz, E. Stathatos, P. Falaras, D.D. Dionysiou, *Catalysis Today* 144 (2009) 19–25;
(b) M. Pelaez, P. Falaras, V. Likodimos, A.G. Kontos, A.A. de la Cruz, K. O'Shea, D. Dionysiou, *Applied Catalysis B: Environmental* 99 (2010) 378–387;
(c) M. Pelaez, P. Falaras, A.G. Kontos, A.A. de la Cruz, K. O'Shea, *Applied Catalysis B: Environmental* 121–122 (2012) 30–39.
- [14] L. Xiang, X. Rongchun, W. Gang, *Catalysis Letters* 125 (2008) 104–109.
- [15] S. Yanfang, X. Tianying, D. Hao, J. Huazi, S. Jianku, Y. Ke, *Journal of Sol–Gel Science and Technology* 52 (2009) 41–48.
- [16] L. Zhou, J. Deng, Y. Zhao, W. Liu, L. An, F. Chen, *Materials Chemistry and Physics* 117 (2009) 522–527.
- [17] C. Yu, J.C. Yu, *Catalysis Letters* 129 (2009) 462–470.
- [18] (a) Y.C. Zhang, J. Li, H.Y. Xu, *Applied Catalysis B: Environmental* 123–124 (2012) 18–26;
(b) N. Wang, L. Zhu, K. Deng, Y. Shec, Y. Yuc, H. Tang, *Applied Catalysis B: Environmental* 95 (2010) 400–407;
(c) G. Colón, M.C. Hidalgo, J.A. Navío, *Langmuir* 17 (2001) 7174–7177;
(d) L. Wang, N. Wang, L. Zhu, H. Yu, H. Tang, *Journal of Hazardous Materials* 152 (2008) 93–98.
- [19] M. Pelaez, N.T. Nolan, S.C. Pillai, M.K. Seery, P. Falaras, A.G. Kontos, P.S.M. Dunlop, J.W.J. Hamilton, J.A. Byrne, *Applied Catalysis B: Environmental* 125 (2012) 331–349.
- [20] G. Barolo, S. Livraghi, M. Chiesa, M.C. Paganini, E. Giamello, *Journal of Physical Chemistry C* 116 (2012) 20887–20894.
- [21] A.E. Giannakas, E. Seristatidou, I. Deligiannakis, I.K. Konstantinou, *Applied Catalysis B: Environmental* 132–133 (2013) 460–468.
- [22] M. Antonopoulou, A. Giannakas, I. Konstantinou, *International Journal of Photoenergy* (2012), <http://dx.doi.org/10.1155/2012/520123>, Article ID 520123.
- [23] A.B. Murphy, *Solar Energy Materials & Solar Cells* 91 (2007) 1326–1337.
- [24] (a) G. Grigoropoulou, K.C. Christoforidis, M. Louloudi, Y. Deligiannakis, *Langmuir* 23 (2007) 10407–10418;
(b) K.C. Christoforidis, M. Louloudi, E.R. Milaeva, Y. Sanakis, Y. Deligiannakis, *Molecular Physics* 105 (2007) 2185–2194.
- [25] J.M. Warman, M.P. de Haas, P. Picbat, N. Serpone, *Journal of Physical Chemistry* 95 (1991) 8858–8861.
- [26] C.P. Poole, *Electron Spin Resonance. A Comprehensive Treatise on Experimental Techniques*, Wiley, New York, 1983.
- [27] N. Wang, Y. Xu, L. Zhu, X. Shen, H. Tang, *Journal of Photochemistry and Photobiology A: Chemistry* 201 (2009) 121–127.
- [28] H.M. Rietveld, *Acta Crystallographica* 22 (1967) 151–152.
- [29] W. Su, Y. Zhang, Z. Li, L. Wu, X. Wang, J. Li, X. Fu, *Langmuir* 24 (2008) 3422–3428.
- [30] (a) C.D. Valentin, E. Finazzi, G. Pacchioni, A. Selloni, S. Livraghi, M.C. Paganini, E. Giamello, *Chemical Physics* 339 (2007) 44–56;
(b) S. Livraghi, A.M. Czoska, M.C. Paganini, E. Giamello, *Chemistry of Materials* 20 (2008) 3706–3714.
- [31] (a) F. Napoli, M. Chiesa, S. Livraghi, E. Giamello, S. Agnoli, G. Granozzi, G. Pacchioni, C. Di Valentin, *Chemical Physics Letters* 477 (2009) 135–138;
(b) S.W. Ahn, K.H. Kang, D.I. Hong, *Journal of Korean Magnetic Resonance Society* 4 (2000) 50–63.
- [32] T. Rajh, A.E. Ostafin, O.I. Micic, D.M. Tiede, M.C. Thurnauer, *Journal of Physical Chemistry* 100 (1996) 4538–4545.
- [33] T. Berger, M. Sterrer, O. Diwald, E. Kno1zinger, D. Panayotov, T.L. Thompson, J.T. Yates Jr., *Journal of Physical Chemistry B* 109 (2005) 6061–6068.
- [34] J.M. Coronado, A.J. Maira, J.C. Conesa, K.L. Yeung, V. Augugliaro, J. Soria, *Langmuir* 17 (2001) 5368–5374.
- [35] Y. Deligiannakis, C. Jegerschisld, A.W. Rutherford, *Chemical Physics Letters* 270 (1997) 564–572.
- [36] (a) J.R. Harbridge, S.S. Eaton, G.R. Eaton, *Journal of Physical Chemistry A* 107 (2003) 598–610;
(b) S.S. Eaton, *Coordination Chemistry Reviews* 83 (1988) 29–72.
- [37] (a) S. Livraghi, M.C. Paganini, E. Giamello, A. Selloni, C. Di Valentin, G. Pacchioni, *Journal of American Chemical Society* 128 (2006) 15666–15671;
(b) S. Livraghi, A. Votta, M.C. Paganini, E. Giamello, *Chemical Communications* 4 (2005) 498–500.
- [38] L.-B. Xiong, J.-L. Li, B. Yang, Y. Yu, *Journal of Nanomaterials* (2012) 13, <http://dx.doi.org/10.1155/2012/831524>, Article ID 831524.
- [39] I. Ross Macdonald, S. Rhydderch, E. Holt, N. Grant, J.M.D. Storey, R.F. Howe, *Catalysis Today* 182 (2012) 39–45.
- [40] T. Velegraki, D. Mantzavinos, *Chemical Engineering Journal* 140 (2008) 15–21.